Article

Insights into the Effect of Trans-to-Cis Photoisomerization of a Co-coordinated Stilbene Derivative on the Luminescence of Di-β-diketonate Lanthanide Complexes

Han Xu,[†] Yu Tan,[†] Ziting Hou, Caiye Fu, and Li-Rong Lin*

Read Online

ACCESS | Metrics & More | Article Recommendations | SI Supporting Information

ABSTRACT: Five lanthanide complexes constructed from a stilbene derivative, (E)-N',N'-bis(pyridin-2-ylmethyl)-4-styrylbenzoyl hydrazide (HL), and two β-diketonates (2-thenoyltrifluoroacetonate, tta), with or without a trifluoroacetate anion ($CF_3CO_2^-$), namely, $[Ln(tta)_2(HL)(CF_3CO_2)]$ $[LnC_{45}H_{32}F_9N_4O_7S_2$, Ln = La (**1**), Nd (**2**), Eu (**3**), or Gd (**4**)] and $[Yb(tta)_2(L)]$ ($YbC_{43}H_{31}F_6N_4O_5S_2$ (**5**), L = deprotonated HL), were synthesized and characterized. Crystals of these five complexes were obtained and analyzed by single-crystal X-ray diffraction. These complexes all belonged to the monoclinic $P2_1/c$ space group. For La^{3+}, Nd^{3+}, Eu^{3+}, and Gd^{3+}, the central lanthanide ion was nine-coordinate with a monocapped twisted square antiprism polyhedron geometry. The central Yb^{3+} ion of complex **5** was eight-coordinate with a distorted double-capped triangular prism polyhedron geometry. Among the five complexes, trans-to-cis photoisomerization of the stilbene group in gadolinium complex **4** showed the largest quantum yield.

Complexes **2**, **3**, and **4** showed dual luminescence and photoisomerization functions. The luminescence change of complex **3** was reversible upon the trans-to-cis photoisomerization process. The sensitization efficiencies of luminescent europium complex **3** in acetonitrile solutions and in the solid state were 49.9 and 42.6%, respectively. These medium sensitization efficiencies led to the observation of simultaneous photoisomerization and luminescence, which further confirmed our previous report that photoisomerization of the stilbene group within complexes was related to the lanthanide ion energy level and whether a ligand-to-metal center or ligand-to-ligand charge-transfer process was present. In complexes **1**−**5**, in addition to the intramolecular absorption transition of the ligand itself (IL, $\pi_{HL}-\pi_{HL}^*$ and $\pi_{tta}-\pi_{tta}^*$), the presence of a ligand-to-ligand charge-transfer transition between tta and HL (LLCT, $\pi_{tta}-\pi_{HL}^*$ or $\pi_{HL}-\pi_{tta}^*$) indicated whether the triplet-state energy of HL was able to transfer to the excited energy level of the lanthanide ions, leading to different extents of HL photoisomerization. These results provide an important route for the design of new dual-function lanthanide-based optical switching materials.
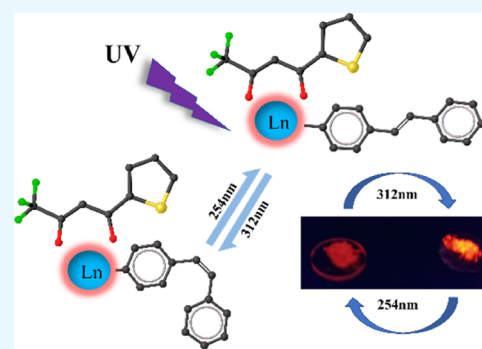
INTRODUCTION

In recent years, smart materials have been studied extensively for their important applications in molecular switches,[1−6] white light-emitting diodes,[7−9] information storage,[10,11] anti-counterfeiting,[12,13] separation and detection,[14−16] drug delivery,[17,18] and other fields.[19−24] Smart material molecules can reversibly change their physical and chemical properties under different external stimuli.[25,26] Among various external stimuli, including light energy, electrical energy, and chemical energy, light is the most suitable and convenient source of clean energy and has advantages of precise control as a stimulus source and energy-saving and environmental protection characteristics. Previously reported light stimulation of smart molecules includes the trans-to-cis isomerization of azobenzene and stilbene derivatives,[27−38] photocyclization of diarylethylenes,[39−41] [2 + 2] cycloaddition of alkenes,[42−44] and [4 + 4] photodimerization of anthracene.[45−48] Photoinduced trans-to-cis isomerization has attracted much attention in inorganic and organic chemistry, materials science, and biology. Photoinduced

trans-to-cis isomerization is the reversible conversion of trans isomers to cis isomers under a certain light wavelength.[27,49] Isomers with different molecular structures have different physical and chemical properties (including magnetic, optical, and electrical properties), which can be controlled by illumination. This feature is widely used in biochemistry, pharmacology, and supramolecular chemistry.[50−56] Much research has been conducted on the photoinduced trans-to-cis isomerization of various azobenzene and stilbene derivatives. In addition, we have studied a series of lanthanide β-diketonate complexes functionalized with azobenzene, finding that azobenzene groups attached to lanthanide β-

diketonate complexes were stable in both solution and the solid state, exhibiting the reversible trans-to-cis photoisomerization properties of azobenzene and good fatigue resistance.[30,34,57,58] The introduction of electron donor substituents is not conducive to improving the photoisomerization quantum yield and photoisomerization rate.[34] Although some ternary complexes of europium and ytterbium β-diketonate complexes functionalized with azobenzene exhibit both luminescence and photoisomerization properties, energy transfer from an azobenzene derivative to lanthanide ions is difficult owing to the first triplet-state energy level of azobenzene derivatives being lower than the excited-state energy level of most lanthanide ions.[57] Therefore, most azobenzene-functionalized lanthanide β-diketonate complexes exhibit photoisomerization but not luminescence emission. Azobenzene-functionalized lanthanide β-diketonate complexes with good dual-function properties are difficult to achieve. To obtain lanthanide complex materials with both luminescent and trans-to-cis photoisomerization properties, we focused on designing stilbene derivatives, which are known for their rich optical properties, such as trans-to-cis photoisomerization, photocyclization, photodimerization, and fluorescence, for introduction into lanthanide β-diketonate complexes.[35] The as-designed stilbene derivative ligand, (E)-N',N'-bis(pyridin-2-ylmethyl)-4-styrylbenzoyl hydrazide (HL), is a tetradentate chelating ligand that can strongly coordinate with lanthanide ions. HL was combined with benzoyl trifluoroacetone (Htfd), a classic β-diketone ligand that sensitizes lanthanide ions, to obtain lanthanide β-diketonate complexes co-coordinated with a stilbene derivative. Stilbene derivative HL co-coordinated in the tfd−lanthanide β-diketonate complex maintained its trans-to-cis photoisomerization properties. The extent of stilbene photoisomerization within complexes was related to the lanthanide ion energy level and whether a ligand-to-metal center or ligand-to-ligand charge-transfer process was present. Trans-to-cis photoisomerization of the stilbene group in the gadolinium complex afforded an approximate fivefold enhancement in the quantum yield compared with HL alone. The Yb and Nd complexes had dual characteristics of infrared luminescence and trans-to-cis photoisomerization. However, in the europium complex, highly efficient ligand energy transfer to the Eu³⁺ ion led to completely suppressed stilbene group photoisomerization. The energy transfer efficiency among ligands HL and tfd and the lanthanide ions affected the lifetime of the lanthanide ion excited-state and photoisomerization behavior of the stilbene group. Therefore, we planned to design and synthesize dual-function materials with photoisomerization properties and excellent optical properties. In this context, we selected 2-thenoyl trifluoroacetone (Htta), a ligand with a better "antenna effect",[59,60] for co-coordination with lanthanide ions to study its luminescence and photoinduced trans-to-cis isomerization and further clarify the relationship between luminescence and isomerization within these complexes.

■ RESULTS AND DISCUSSION

X-ray Crystallographic Analysis. Crystals of the five complexes were obtained by slow evaporation from a methanol solution over 1 week. Crystal analysis showed that the five complexes had similar structures and all belonged to the monoclinic $P2_1/c$ space group. For complexes **1−4**, the central lanthanide ion was coordinated with six oxygen atoms and three nitrogen atoms to form a stable nine-coordinate structure

with monocapped twisted square antiprism polyhedron geometry. HL is a tetradentate ligand that provides one oxygen atom and three nitrogen atoms as chelating atoms. The other four chelating oxygen atoms were provided by two 2-thenoyltrifluoroacetonate (tta) ligands, while the sixth oxygen was derived from the trifluoroacetate anion hydrolyzed by the ligand Htta. In complexes **1−4**, intermolecular hydrogen bonding existed between the carbonyl oxygen of trifluoroacetate and hydrogen on the hydrazine nitrogen in HL. The coordination mode of complex **5** was slightly different from those of complexes **1−4**, with the central Yb(III) ion having a coordination number of 8 with a distorted double-capped triangular prism polyhedron geometry. No trifluoroacetate anion was involved in coordination in **5** owing to removal of a proton from the hydrazine nitrogen in HL to balance the charge. This was similar to our previously reported Yb³⁺ complexes functionalized by azobenzene groups.[58] The crystal structures of complexes **4** and **5** are shown in Figure 1, while
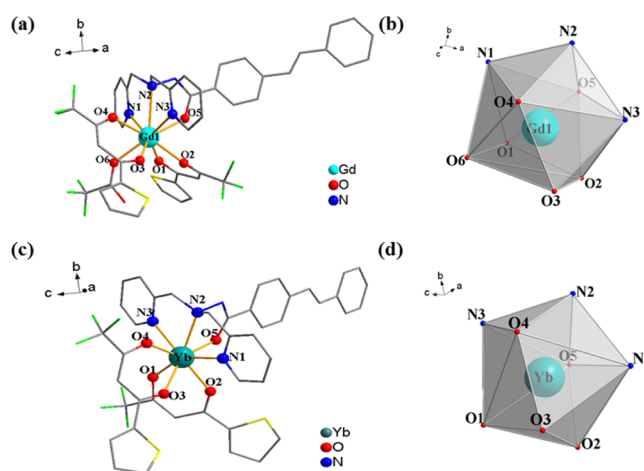
Figure 1. Crystal structures of complexes **4** (a) and **5** (c) (all hydrogen atoms are omitted for clarity) and coordination polyhedron geometry of central La(III) (b for complex **4**, d for complex **5**).

those of complexes **1−3** are shown in Figure S1 in the Supporting Information. The crystallographic parameters of complexes **1−5** are provided in Table 1, while selected bond lengths and angles are shown in Tables S1 and S2 (Supporting Information). The lanthanide ion−oxygen bond length ranges in complexes **1−5** were 2.468−2.537, 2.357−2.451, 2.371−2.425, 2.377−2.465, and 2.206−2.475 Å, respectively. The corresponding lanthanide ion−nitrogen bond length ranges were 2.734−2.873, 2.644−2.755, 2.639−2.752, 2.613−2.706, and 2.475−2.546 Å, respectively. These results were within the ranges of reported lanthanide β−diketonate complexes.[30,34,58] The measured XRD powder diffraction spectra of complexes **1−5** were in agreement with the simulated values (Figure S2 in the Supporting Information), confirming that the obtained five complexes had a pure phase.

Thermal Analysis of Complexes 1−5. Thermogravimetric analyses (TGAs) of complexes **1−5** were conducted using powder samples in the temperature range of 30−800 °C under a nitrogen atmosphere. The TGA plots showed that complexes **1−4** had similar thermal decomposition processes, with complex **5** also showing the same trend (Figure S3 in the Supporting Information). Complexes **1−4** underwent the first stage of decomposition in the temperature range of 255−380

Table 1. Crystallographic Data for Complexes 1−5

crystal data	1	2	3	4	5
formula	LaC$_{45}$H$_{32}$F$_9$N$_4$O$_7$S$_2$	NdC$_{45}$H$_{32}$F$_9$N$_4$O$_7$S$_2$	EuC$_{45}$H$_{32}$F$_9$N$_4$O$_7$S$_2$	GdC$_{45}$H$_{32}$F$_9$N$_4$O$_7$S$_2$	YbC$_{43}$H$_{31}$F$_6$N$_4$O$_5$S$_2$
FW	1114.77	1122.13	1127.82	1133.11	1034.88
crystal system	monoclinic	monoclinic	monoclinic	monoclinic	monoclinic
space group	$P2_1/c$	$P2_1/c$	$P2_1/c$	$P2_1/c$	$P2_1/c$
a (Å)	9.891(5)	24.269(4)	24.1658(4)	9.762(4)	8.308 (10)
b (Å)	17.372(10)	9.788(2)	9.7895(2)	17.811(6)	26.613(4)
c (Å)	30.071(2)	19.295(4)	19.2341(4)	32.585(17)	18.586(3)
α (°)	90	90	90	90	90
β (°)	93.666(6)	101.887(2)	101.285(2)	111.049(5)	95.7(10)
Γ (°)	90	90	90	90	90
V (Å)	5157.0(5)	4485.4(2)	4462.26(15)	5288.0(4)	4089.5(10)
Z	4	4	4	4	4
D (g cm^{-3})	1.436	1.659	1.679	1.423	1.681
θ range (°)	5.87 to 133.07	7.44 to 133.20	7.46 to 131.338	5.75 to 129.99	6.64 to 154.78
refl. col.	29078	28401	31102	29121	28488
data/res./para.	8837/1078/733	7912/1029/787	7585/924/761	8958/733/698	8299/282/624
GOF	1.044	1.054	1.162	1.057	1.027
final R	$R_1 = 0.0889$	$R_1 = 0.0922$	$R_1 = 0.0518$	$R_1 = 0.1001$	$R_1 = 0.0351$
R (all data)	$R_1 = 0.1585$, w$R_2 =$ 0.1373	$R_1 = 0.1082$, w$R_2 =$ 0.2544	$R_1 = 0.0627$, w$R_2 =$ 0.1401	$R_1 = 0.1229$, w$R_2 =$ 0.3024	$R_1 = 0.0444$, w$R_2 =$ 0.0903

°C with mass losses of 27.05, 27.92, 27.65, and 27.67%, respectively. These results were similar to theoretically calculated percentages for the loss of one trifluoroacetate anion and one tta dionate from the complexes (29.98, 29.84, 29.63, and 29.47%, respectively). Meanwhile, the TGA curves of complex **5** showed a first-stage mass loss of 24.23% in the temperature range of 270−370 °C, indicating a mass loss of one tta dionate from the complex (calculated, 23.43%). All complexes further decomposed between 380 and 800 °C. These thermal stability results showed that the trifluoroacetate anion and tta dionate were more readily removed from the complexes, indicating that HL was a strongly coordinating tetradentate ligand for chelating lanthanide ions.

Magnetic Properties of Complex 4. The magnetic properties of complex **4** were also studied. Variable temperature molar magnetic susceptibility (χ_M) in the range of 2−300 K was measured under an applied field of 1000 Oe (Figure S4 in the Supporting Information). The room-temperature χ_MT value was 7.42 cm^3 K mol^{-1}, which was slightly lower than the theoretical value (7.87 for one isolated Gd^{3+} ion) owing to quenching of the orbital magnetic moment contribution to the center ion. The values of C (cm^3 K mol^{-1}) and θ (K) obtained from the best fit χ_MT data (χ_M^{-1} vs T) using the Curie−Weiss equation were 7.14 and −0.77, respectively, showing the presence of a weak antiferromagnetic interaction between Gd^{3+} ions.[61,62]

Photoisomerization Behavior of Complexes 1−5. UV−vis absorption spectra of Htta, HL, and their complexes **1−5** in acetonitrile at room temperature were obtained, with the corresponding spectral data listed in Table 2. The spectral shapes of complexes **1−5** showed iteration of the free ligand Htta and HL absorption spectra (Figure 2), with a red shift of about 20 nm at the long wavelength and a small shift at the short wavelength compared with free ligands. The molar absorption coefficients of complexes **1−5** at the maximum wavelength were in the same order as those of the free ligands. However, the results for complex **1** were higher than those of the free ligands, perhaps owing to the rigid structure resulting

Table 2. UV−Vis Absorption Data of Ligands and Complexes 1−5 in Acetonitrile Solutions

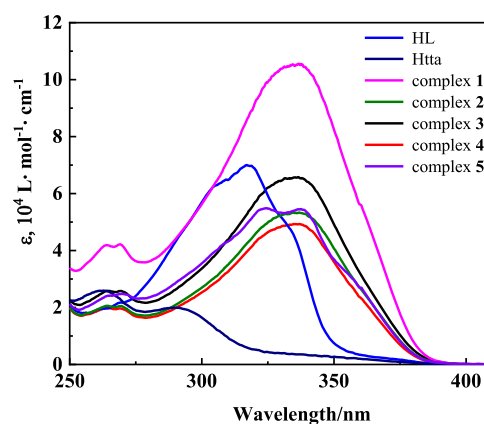| compounds	λ_{max}[nm] (ε_{max}[10^4 L·mol^{-1}·cm^{-1}])	
Htta	292(1.95)	262(2.64)
HL	317(5.16)	262(1.96) 268(2.13)
1	335(10.50)	269(4.14)
2	337(5.14)	269(2.04)
3	335(6.52)	269(2.59)
4	336(4.94)	270(1.91)
5	337(5.44)	269(2.45)

Figure 2. UV−vis absorption spectra of Htta, HL, and complexes **1−5** in acetonitrile solutions.

from the coordination effect of the lanthanum ion with no f electrons. Density functional theory (DFT)/time-dependent (TD)−DFT calculations (Table 5) showed that complex **1** has the largest oscillator strengths for the intramolecular charge transition of the ligands (IL, $\pi_{HL}-\pi_{HL}^*$), ligand-to-ligand charge transfer (LLCT, $\pi_{HL}-\pi_{tta}^*$), and ligand-to-metal certer charge transfer (L$_{HL}$MCT) transitions among the five complexes. This might be the reason that complex **1** shows a different behavior.

The five complexes were similar to our previously reported lanthanide complexes, with only the two trifluoro-1-phenyl-butanedionate (tfd) ligands changed to tta ligands, but they showed very different photoisomerization properties. The five complexes showed similar photoisomerization behavior in acetonitrile solutions but different photoisomerization rates and quantum yields. For example, the UV−vis absorption spectra of complex **3** in acetonitrile solutions showed a similar variation to that of free ligand HL. In acetonitrile solutions, under 312-nm UV light irradiation, the characteristic absorption peak intensity of the $\pi-\pi^*$ transition at 335 nm gradually decreased with increasing irradiation time. Simultaneously, the characteristic absorption peak intensity of the $\pi-\pi^*$ transition at 269 nm gradually increased, with an isosbestic point appearing at 287 nm (Figure 3). Complex **3**
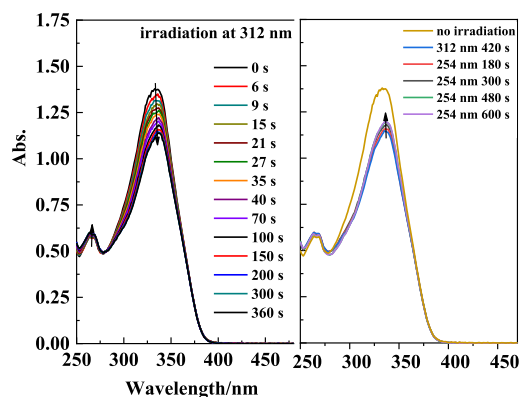

Figure 3. UV−vis spectral change of complex **3** in acetonitrile solutions (2.0×10^{-5} mol/L) upon irradiation at UV-312 nm and recoverable irradiation at UV-254 nm as a function of time.

reached a photostable state after irradiation for 300 s. The solution was then subjected to 254 nm UV light irradiation, which caused the characteristic absorption peak intensity at 335 nm to increase with increasing irradiation time, with a constant intensity maintained after 600 s. These changes indicated that the stilbene group in the complex underwent a trans−cis−trans photoisomerization process.

Subsequently, the reversibility and recyclability of the trans−cis−trans photoisomerization behavior of complex **3** in acetonitrile solutions were tested. UV−vis absorption spectra of the solution were recorded alternately using 312 nm UV light irradiation for 3 min followed by 254 nm UV light for 5 min. As shown in Figure 4, the trans-to-cis photoisomerization reaction of complex **3** was reversible and recyclable. Although both the pure ligand and complex **3** underwent photolysis, the number of cycles for complex **3** under an alternating UV light irradiation was higher than that of the pure HL ligand owing to the enhanced photostability of the stilbene group after complex formation.

The photoisomerization properties of the four other complexes were also explored, showing similar photoisomerization behavior in acetonitrile solutions but with different photoisomerization quantum yields and rate constants. From variations in the UV absorption spectra with increasing irradiation time, the trans-to-cis photoisomerization quantum yields and first-order kinetic rate constants were determined. The UV−vis spectra of the other four complexes in acetonitrile solutions under alternating irradiation with UV light at 312 and 254 nm are shown in Figures S5 and S6 (Supporting
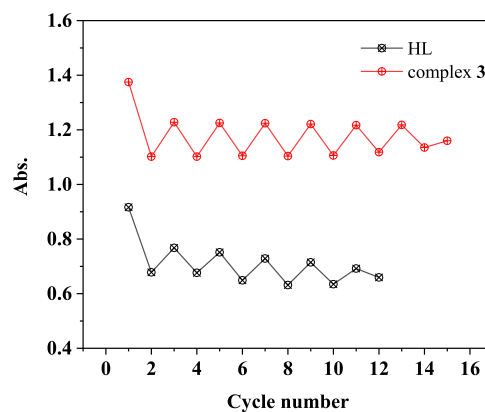
Figure 4. Cycles of maximum absorption intensity at 335 nm of complex **3** and 317 nm of HL in acetonitrile solutions are modulated by the irradiation of UV light at 312 nm for 3 min and 254 nm for 5 min, alternately.

Information). Table 3 shows the trans-to-cis quantum yields (Φ_{t-c}) under irradiation at 312 nm and photoisomerization

Table 3. Photoisomerization Rate Constants K_{iso} (s^{-1}) and Quantum Yields (Φ_{t-c}) of HL and Complexes 1−5 in Acetonitrile Solutions

compounds	$10^3\,k_{iso}$	$10^2\Phi_{t\rightarrow c}$	$R_1{}^a$	$R_2{}^a$	$R_1{}^{a,c}$	$R_2{}^{a,c}$
HL	4.8 ± 0.5	1.9 ± 0.1	1.0	1.0	1.0	1.0
1	12.9 ± 0.2	1.9 ± 0.1	2.7	1.0	0.1	1.0
2	15.1 ± 0.5	3.3 ± 0.3	3.1	1.7	3.4	2.0
3	23.2 ± 1.8	10.4 ± 0.3	4.8	5.5	^{b}	^{b}
4	33.7 ± 2.4	10.9 ± 0.3	7.0	5.7	4.8	4.5
5	17.3 ± 0.3	5.7 ± 0.3	3.6	3.0	1.3	1.2

^{a}R$_1$ is the ratio of the K_{iso} value of a complex to HL and R$_2$ is the ratio of the $\Phi_{t\rightarrow c}$ value of a complex to HL. ^{b}No detectable value for complex **3** in ref 35. ^{c}Data calculated from ref 35.

rate constants (k, s^{-1}) of HL and complexes **1−5** in acetonitrile (UV light power, 266 μW cm^{-2} at 312 nm). Although nuclear magnetic resonance (NMR) spectroscopy can be used to obtain an accurate quantum yield,[63,64] the quantum yields herein, calculated using only the UV−vis spectrum variations, were "apparent". These calculations were performed using the same method as in our previous report.[34] The photoisomerization quantum yields of the complexes were all higher than that of HL, while their isomerization rate constants (k_{iso}) were positively correlated with the photoisomerization quantum yields. The photoisomerization rate constant and quantum yield of complex **4** were largest among the five complexes. This was similar to our previously reported 4,4,4-trifluoro-1-phenylbutane-1,3-diketonate gadolinium complex co-coordinated with a stilbene derivative ([Gd(tfd)$_2$(HL) (CF$_3$COO)]).[35] However, the photoisomerization rate constants (k_{iso}) and quantum yields (Φ_{t-c}) of the five complexes and HL were in the order of **4** > **3** > **5** > **2** > **1** > HL. Complex **3** was different from the reported 4,4,4-trifluoro-1-phenyl-butane-1,3-diketone europium complex co-coordinated with a stilbene derivative ([Eu(tfd)$_2$(HL) (CF$_3$COO)]), which exhibited no detectable photoisomerization. This was due to the difference in energy transfer efficiency between the ligand and lanthanide ion, which will be discussed below in the studies on photoluminescence properties and theoretical calculations.

Photoluminescence Properties of Complexes 2, 3, and 5. Nd^{3+}, Eu^{3+}, and Yb^{3+} β-diketonate complexes are known to emit strong red or near-infrared (NIR) luminescence if efficient energy transfer from the β-diketonate and auxiliary ligands to the central lanthanide(III) ions is present. First, the luminescence properties of complex **3** at room temperature were investigated. Photoluminescence spectra of complex **3** in acetonitrile solutions and in the solid state are shown in Figure 5. Complex **3** displayed pure red photoluminescence and its
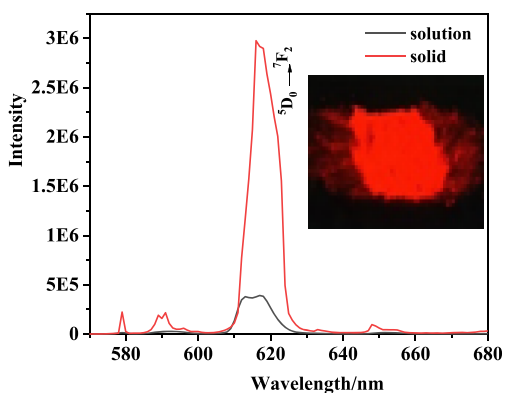
Figure 5. Luminescence spectra of complex **3** in acetonitrile solutions (2.0 × 10⁻⁵ mol/L) and in the solid state (λ_{ex} = 355 nm). The inset shows images of a bright red color luminescence in the solid state under a 365 nm UV lamp.

CIE coordinate was x = 0.67 and y = 0.33 (Figure S7 in the Supporting Information). Upon excitation at 355 nm, complex **3** exhibited characteristic Eu(III) ion emission bands of $^5D_0 \rightarrow$ ^7F_J (J = 0−4) transitions. The $^5D_0 \rightarrow$ $^7F_2$ transition at 614 nm from the induced electric dipole hypersensitive transition was strongest and dominated the whole spectrum. The $^5D_0 \rightarrow$ $^7F_{0,1,3}$ transitions at 578, 590, and 650 nm, respectively, were relatively weak. Only one peak for the $5D_0 \rightarrow 7F_0$ (0−0) transition and three Stark components for the magnetic dipole $5D_0 \rightarrow 7F_1$ transition, in particular the splitting pattern of $5D_0 \rightarrow 7F_2$ in the emission spectra, suggested the major presence of a single chemical environment around the Eu(III) ion and lower complex symmetry. The overall luminescence quantum yields (Φ_{tot}) of complex **3** were determined experimentally to be 0.21 and 0.39 in acetonitrile solutions and in the solid state, respectively, at room temperature, which were slightly higher than those of complex $[Eu(tfd)_2(HL)(CF_3COO)]$ with a similar structure (Φ_{tot} = 0.19 in acetonitrile and 0.22 in solid). Furthermore, the $5D_0$ emission decay curve excited at 355 nm showed a single exponential behavior monitored within the $5D_0 \rightarrow 7F_2$ transition (Figure S8 in the Supporting Information), yielding lifetimes (τ_{obs}) of 616 and 765 μs in acetonitrile solutions and in the solid state, respectively. The radiation life time (τ_{rad}) of Eu^{3+} ions can be calculated using eq 1[65]

$$\frac{1}{\tau_{rad}} = A_{MD,0} \times n^3 \times \frac{I_{tot}}{I_{MD}} \qquad (1)$$

where $A_{MD,0}$ is the spontaneous emission probability of the $^5D_0 \rightarrow {}^7F_1$ transition *in vacuo* (14.65 s⁻¹), I_{tot} is the total integral of the whole emission spectrum, I_{MD} is the integral of the $^5D_0 \rightarrow {}^7F_1$ transition emission peak, and n is the refractive index of the solvent (1.5 in the solid state).

Therefore, using the equation $\Phi_{Ln} = \tau_{obs}/\tau_{rad}$,[65] the intrinsic quantum yields (Φ_{Ln}) in acetonitrile solutions and in the solid state were calculated to be 42.4 and 91.5%, with sensitization efficiencies ($\eta_{sen} = \Phi_{tot}/\Phi_{Ln}$) of 49.9 and 42.6%, respectively (Table 4). These lower sensitization efficiencies indicated that

Table 4. Luminescence Physical Parameters of Complexes 2, 3, and 5

complex	environment	τ_{obs} (μs)	τ_{rad} (μs)	Φ_{tot} (%)	Φ_{Ln} (%)	η_{sens} (%)
2	solution Solid	3.2			1.3	
	solid	6.1			2.4	
3	solution	616	1452	21.10	42.4	49.9
	solid	765	835	38.94	91.5	42.6
5	solution	12.1			0.6	
	solid	14.3			0.7	

the ligand energy transfer to the Eu^{3+} ion was still less efficient in this complex, with sufficient energy remaining for HL to undergo trans-to-cis photoisomerization. This explained why photoisomerization of the stilbene group was observed in complex **3** but suppressed complex $[Eu(tfd)_2(HL)(CF_3COO)]$ with a similar structure, which exhibited a higher sensitization efficiency of 97.9% in acetonitrile solutions and 96.7% in the solid state, resulting in almost no energy remaining for HL to undergo trans-to-cis photoisomerization.

Furthermore, the emission of complex **3** in the photostationary cis form in the solid state was checked (Figure 6).
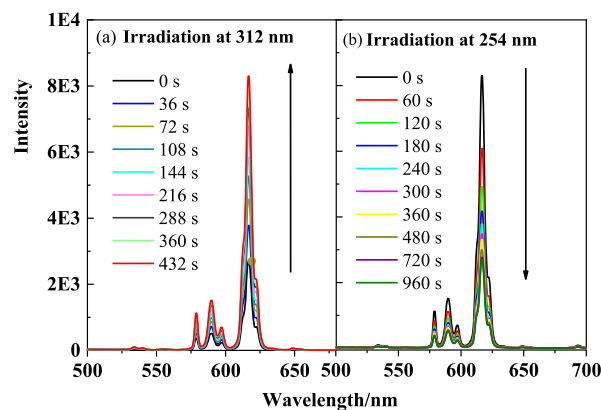
Figure 6. Luminescence spectral change of complex **3** in the solid state upon irradiation at UV-312 nm (a) and recoverable irradiation at UV-254 nm (b) as a function of time.

Under irradiation at 312 nm, the luminescence intensity of $^5D_0 \rightarrow {}^7F_J$ (J = 0−4) transitions of complex **3** all increased with increasing irradiation time. The photoisomerization reaction reached a photostable state after 5 min. The powder was then irradiated with UV light at 254 nm, which gradually decreased the luminescence intensity with increasing irradiation time, finally reaching a new photostable state after 15 min. The changes in luminescence intensity with trans-to-cis photoisomerization of complex **3** were also reversible and recyclable and observed for more than 20 cycles with small photolysis (Figure S9 in the Supporting Information). A similar luminescence change was also observed for complex **3** in acetonitrile solutions (Figure S10 in the Supporting Information). This luminescence variation might result from a new crystal packing within the cis form, introducing the

hypersensitive transition enhancement in complex **3**. These results show that complex **3** is a new lanthanide-based optical switching material.

The NIR luminescence of complexes **2** and **5** in acetonitrile solutions and in the solid state was also examined. With excitation wavelengths set at 358 and 365 nm, respectively, complexes **2** and **5** showed luminescence peaks characteristic of Yb^{3+} and Nd^{3+} ions, respectively (Figure 7). The strong
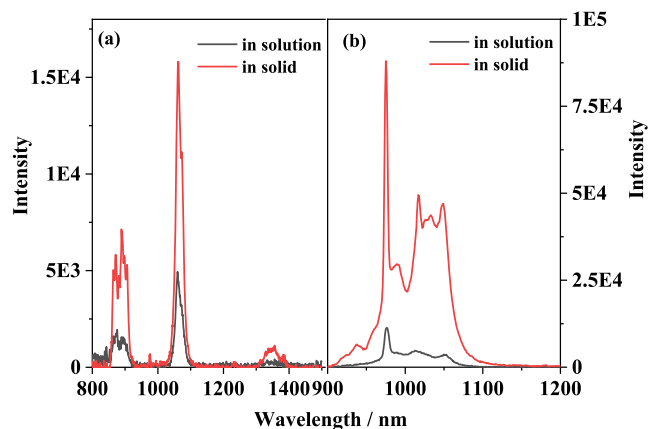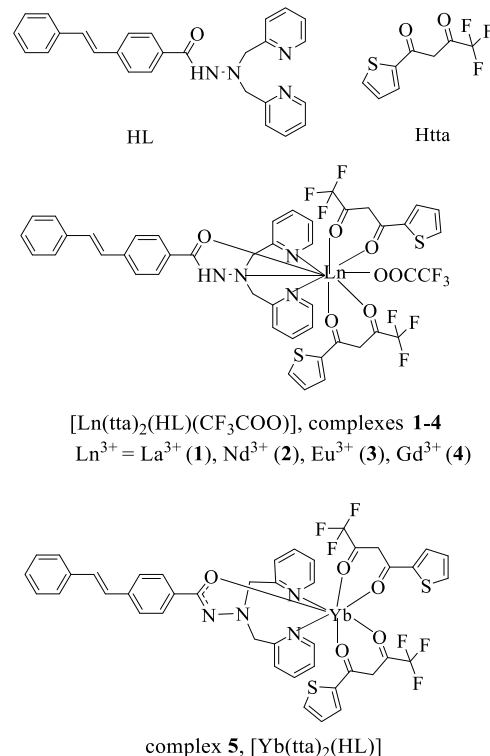

Figure 7. NIR luminescence spectra of complexes **2** (a, λ_{ex} = 365 nm) and **5** (b, λ_{ex} = 358 nm) in acetonitrile solutions (1.0×10^{-4} mol/L) and in the solid state.

luminescence emission peak of complex **2** was located at about 1062 nm, which corresponded with the $^4F_{3/2} \rightarrow {}^4I_{11/2}$ transition of Nd^{3+} ions. The weak and broad emission peaks at 887 and 1335 nm corresponded to $^4F_{3/2} \rightarrow {}^4I_{9/2}$ and $^4F_{3/2} \rightarrow {}^4I_{13/2}$ transitions, respectively. Complex **5** also showed three luminescence emission peaks, among which the emission at 980 nm was strongest, attributed to the $^2F_{5/2} \rightarrow {}^2F_{7/2}$ transition of Yb^{3+} ions, while the broad emission peaks at around 1015 and 1050 nm were attributed to the Stark splitting of the $^2F_{7/2}$ multiplex.

The NIR intrinsic quantum yield of the lanthanide ions can be estimated using the equation $\Phi_{Ln} = \tau_{obs}/\tau_0$, where τ_0 is the natural lifetime (0.25 ms for Nd^{3+} and 2.0 ms for Yb^{3+}).[66,67] The luminescence lifetime (τ_{obs}) and intrinsic quantum yield (Φ_{Ln}) of complexes **2** and **5** are shown in Table 4. The decay curves of the strongest peaks of complexes **2** and **5** as a function of time, which fitted a single exponential behavior, were used to calculate τ_{obs}, as shown in Figure S11 (Supporting Information). The NIR luminescence properties of the two complexes were similar to our reported Nd^{3+} and Yb^{3+} complexes with similar structures, which also had observed lifetime values in the order of 1−10 μs.[35] This indicated that the energy transfer efficiency of the two series of complexes was similar. Therefore, the photoisomerization rates and quantum yields of the two series of Nd and Yb complexes were also similar. The triplet excited-state energy levels ($3\pi\pi^*$) of ligands can be determined from the phosphorescence spectra of their corresponding Gd complexes.[68] HL did not show phosphorescence at room temperature. The phosphorescence of Htta, Htfd, and their Gd complexes at room temperature was measured, with ligands and their complexes showing the same maximum emission wavelength of around 20,202 cm^{-1} for Htta and 21,413 cm^{-1} for Htfd (Figure S12), respectively, in agreement with the literature.[69] The triplet energy of HL estimated by TD−DFT was 18,083 cm^{-1}. The

energy levels of ligands HL, Htta, and Htfd and lanthanide ions Eu^{3+}, Nd^{3+}, Yb^{3+}, and Gd^{3+} are shown in Scheme 2. All triplet

Scheme 1. Schematic Structures of Complexes 1−5

$[Ln(tta)_2(HL)(CF_3COO)]$, complexes **1-4**
Ln^{3+} = La^{3+} (**1**), Nd^{3+} (**2**), Eu^{3+} (**3**), Gd^{3+} (**4**)

complex **5**, $[Yb(tta)_2(HL)]$

Scheme 2. Schematic Representation of Energy Levels of the First Excited States of Ligands HL, Htta, and Htfd and the Related Energy Levels of Eu^{3+}, Nd^{3+}, Yb^{3+}, and Gd^{3+}
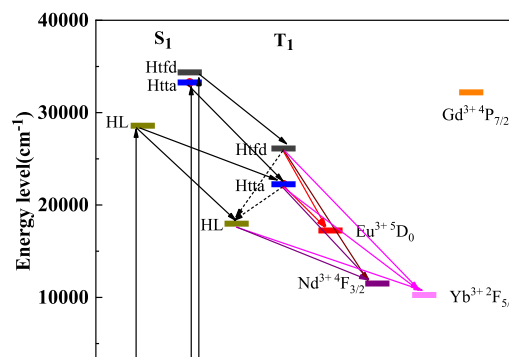
energy levels of ligands were higher than the Eu^{3+} $5D_0$ (17,241 cm^{-1}), Nd^{3+} $4F_{3/2}$ (11,500 cm^{-1}), and Yb^{3+} $2F_{5/2}$ (10,260 cm^{-1}) energy levels. HL might directly transfer energy to lanthanide ions through the triplet excited state. This explains why the stilbene-attached lanthanide β-diketonate complexes showed stronger luminescence than azobenzene-functionalized lanthanide complexes.

Electronic Absorption Analysis. Complexes **1−5** in the acetonitrile solvent were successfully optimized using DFT, with the optimized structural geometric parameters shown in Tables S3 and S4. The optimized partial bond lengths and angles were compared with those obtained by X-ray single-crystal diffraction (measured crystal data shown in Tables S1 and S2, Supporting Information), showing some differences. The optimized lanthanide ion−oxygen bond length ranges in
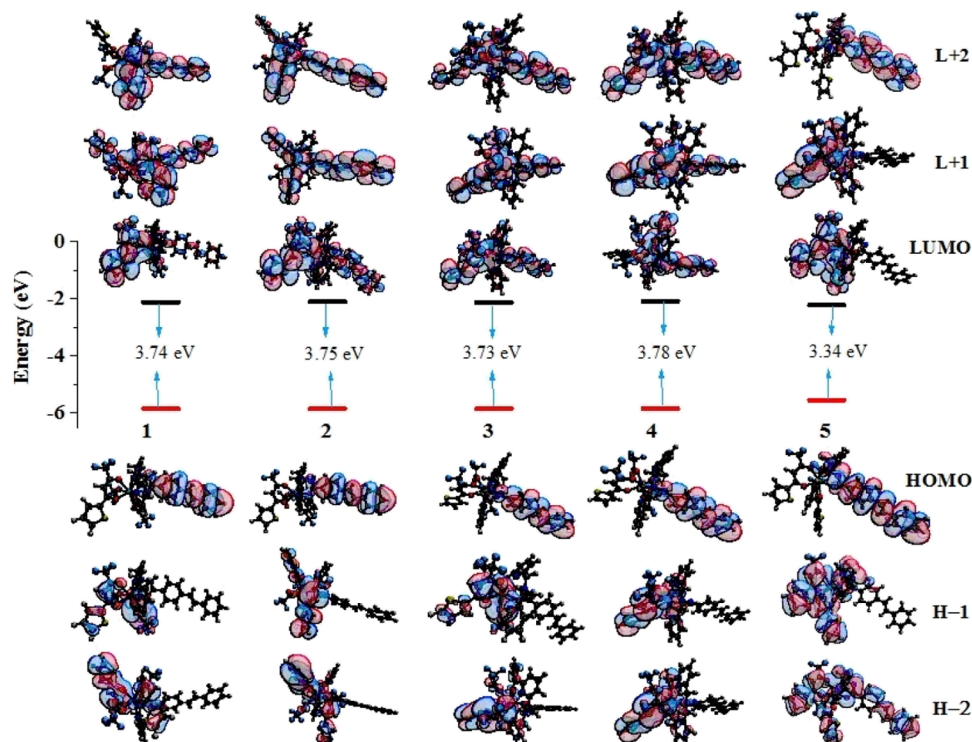
Figure 8. HOMO and LUMO energy levels and orbital distributions of complexes **1−5**. Most relevant MOs of complexes **1−5** associated with vertical excitation are shown in Table 5.

complexes **1−5** were 2.463−2.560, 2.386−2.445, 2.337−2.467, 2.322−2.470, and 2.229−2.263 Å, respectively. The corresponding lanthanide ion−nitrogen bond length ranges were 2.813−2.998, 2.729−2.779, 2.712−2.901, 2.719−2.918, and 2.522−2.585 Å, respectively. They are close to the crystal data (in crystal, Ln−O bond length ranges in complexes **1−5** were 2.468−2.537, 2.357−2.451, 2.371−2.425, 2.377−2.465, and 2.206−2.475 Å, respectively. The Ln−N bond length ranges were 2.734−2.873, 2.644−2.755, 2.639−2.752, 2.613−2.706, and 2.475−2.546 Å, respectively). These differences were within a reasonable range and acceptable for the simulation process conducted on the acetonitrile solution, while experimental data were obtained in the crystal state. The calculated bond lengths and angles were essentially consistent with the measured bond lengths and angles, confirming the rationality of the large-core effective core potentials (ECPs).

Electron density distributions of the highest occupied molecular orbitals (HOMOs) and lowest unoccupied molecular orbital (LUMO) of complexes **1−5** in the acetonitrile solvent were obtained, as shown in Figure 8. Among them, complexes **2**, **4**, and **5** were optimized using the UB3LYP functional and only their α-orbitals were shown. The HOMOs of the five complexes had similar orbital distributions and were mainly distributed on the stilbene group of ligand HL, while the LUMOs showed slight differences. Complexes **2**, **3**, and **4** showed similar LUMO distributions, with LUMOs mainly distributed on the two tta ligands, the stilbene group of ligand HL, and partially on the central lanthanide ion. Meanwhile, the LUMO of complex **1** was mainly distributed on the two tta ligands, partially distributed on the central lanthanide ion, and slightly distributed on the stilbene group of ligand HL. The LUMO of complex **5** was mainly distributed on the two tta ligands and partially distributed on the central Yb^{3+} ion, with no electron density on the stilbene group of ligand HL. The

LUMOs +1 and +2 of complexes **1−4** all had similar electron density distributions on the two tta ligands, stilbene group of HL, and was partially on the central metal. Furthermore, the HOMOs −1 and −2 of complexes **1−4** all pull electron density away from the HL group toward the two tta ligands and partially toward the central metal. Although the LUMOs showed slight differences among the five complexes, the HOMO and LUMO energy levels were close to each other, with only complex **5** showing a small gap.

Based on the optimized geometric structure, electron absorption spectra calculated by TD−DFT were compared with those obtained experimentally. The simulated electronic absorption spectra are shown in Figure S13 (Supporting Information). The strongest absorption peaks of the five complexes in the acetonitrile solution obtained experimentally were all observed at around 335 nm, while the absorption peaks calculated by the polarized continuum model (PCM) simulation in the acetonitrile solvent were all around 345 nm. The simulated electronic absorption spectra were close to the experimental data. The solvent-corrected main transition energies (eV), with contributing excitation (%), oscillator strengths (f, only showing $f > 0.1$), associated wavelengths (λ), and dominant excitation character, are shown in Table 5. Complexes **1−4** showed similar mixed transitional characteristics. TD−DFT/PCM calculations showed that the absorption band in the range of 230−400 nm measured experimentally mainly originated from the IL ($\pi_{HL} \rightarrow \pi_{HL}^*$ and $\pi_{tta} \rightarrow \pi_{tta}^*$), LLCT ($\pi_{HL} \rightarrow \pi_{tta}^*$ or $\pi_{tta} \rightarrow \pi_{HL}^*$), and a small charge-transfer transition from ligands to the central Ln^{3+} ion (LMCT). As shown in Table 3, the photoisomerization rate constants and quantum yields of complexes **1−4** evidently increased with increasing atomic number from La to Gd. Among the four complexes, complex **3** was rather different from our previously reported [Eu(tfd)$_2$(HL) (CF$_3$COO)]

Table 5. Solvent-Corrected (Acetonitrile) Major Transition Energies (eV) to Excited States of HL and Complexes 1−5 with Contributing Excitation (%), Oscillator Strengths (f), Associated wavelengths (λ), and Dominant Excitation Characteristics

compounds	transition	f	E/ev	λ/nm	character
complex 1	HOMO → LUMO (18%), HOMO → L + 1 (79%)	0.594	3.45	359	IL(π_{HL}–π^*_{HL})LLCT(π_{HL}–π^*_{tta})L_{HL}MC′
	HOMO → L + 2 (95%)	0.678	3.54	350	IL(π_{HL}–π^*_{HL})LLCT(π_{HL}–π^*_{HL})L_{HL}MC′
	H − 1 → L + 1 (92%)	0.152	3.64	341	IL(π_{tta}–π^*_{tta})LLCT(π_{tta}–π^*_{HL})L_{tta}MCT
	H − 2 → L + 1 (87%)	0.301	3.71	334	IL(π_{tta}–π^*_{tta})LLCT(π_{tta}–π^*_{HL})L_{tta}MCT
	H − 1 → L + 2 (74%), H − 2 → L + 1 (12%)	0.434	3.78	328	IL(π_{tta}–π^*_{tta})LLCT(π_{tta}–π^*_{HL})L_{tta}MCT
complex 2	HOMO(A) → LUMO(A) (64%)	0.185	3.35	370	IL(π_{HL}–π^*_{HL})LLCT(π_{HL}–π^*_{tta})L_{HL}MC′
	H − 1(A) → L + 2(A) (13%)	0.118	3.43	361	IL(π_{tta}–π^*_{tta})LLCT(π_{tta}–π^*_{HL})L_{tta}MCT
	HOMO(A) → L + 2(A) (20%)	0.141	3.49	355	IL(π_{HL}–π^*_{HL})LLCT(π_{HL}–π^*_{tta})L_{tta}MCT
	HOMO(A) → L + 2(A) (25%)	0.485	3.53	351	IL(π_{HL}–π^*_{HL})LLCT(π_{HL}–π^*_{tta})L_{tta}MCT
	HOMO(A) → L + 4(A) (22%),	0.187	3.74	331	IL(π_{HL}–π^*_{tta})L_{HL}MCT
	H − 2(A) → L + 1(A) (17%)				IL(π_{HL}–π^*_{tta})LLCT(π_{tta}–π^*_{HL})
	H − 1(A) → L + 4(A) (24%)	0.254	4.29	289	IL(π_{HL}–π^*_{tta})L_{tta}MCT
complex 3	HOMO → LUMO (18%), H − 2 → LUMO (11%)	0.245	3.40	364	IL(π_{HL}–π^*_{HL})LLCT(π_{HL}–π^*_{tta})L_{HL}MC′
	H − 2 → L + 2 (22%), H − 2 → L + 3 (13%)				IL(π_{HL}–π^*_{tta})LLCT(π_{tta}–π^*_{HL})
	HOMO → LUMO (28%), H − 2 → L + 2 (13%)	0.222	3.42	362	IL(π_{HL}–π^*_{HL})LLCT(π_{HL}–π^*_{tta})L_{HL}MC′
	H − 1 → L + 3 (12%)				IL(π_{tta}–π^*_{tta})LLCT(π_{tta}–π^*_{HL})L_{tta}MCT
	HOMO → L + 2 (50%), H − 1 → L + 6 (12%)	0.292	3.51	353	IL(π_{HL}–π^*_{HL})LLCT(π_{HL}–π^*_{tta})L_{HL}MC′
	H − 1 → L + 5 (17%), H − 1 → L + 6 (37%),	0.139	3.53	351	IL(π_{tta}–π^*_{tta})L_{tta}MCT
	HOMO → L + 2 (16%)				IL(π_{tta}–π^*_{tta})LLCT(π_{tta}–π^*_{HL})L_{tta}MCT
	HOMO → L + 3 (93%)	0.309	3.59	345	IL(π_{HL}–π^*_{HL})LLCT(π_{HL}–π^*_{tta})L_{HL}MC′
	H − 2 → L + 1 (32%), H − 2 → L + 5 (11%),	0.191	3.80	326	IL(π_{HL}–π^*_{HL})LLCT(π_{HL}–π^*_{tta})L_{HL}MC′
	H − 2 → L + 6(22%)				
	H − 1 → L + 2 (18%), H − 1 → L + 4 (16%),	0.264	3.84	323	IL(π_{tta}–π^*_{tta})LLCT(π_{tta}–π^*_{HL})L_{tta}MCT
	H − 1 → L + 5 (11%)	0.402	3.55	349	
complex 4	HOMO (A) → L + 1 (A) (27%)	0.349	3.57	347	IL(π_{HL}–π^*_{HL})LLCT(π_{HL}–π^*_{tta})L_{HL}MC′
	HOMO (A) → LUMO (A) (13%)				IL(π_{HL}–π^*_{HL})LLCT(π_{HL}–π^*_{tta})L_{HL}MC′
	HOMO (A) → L + 1 (A) (21%), HOMO (A) → L + 2 (A)				
	H − 1 (A) → LUMO (A) (54%),	0.101	3.63	341	IL(π_{tta}–π^*_{tta})LLCT(π_{tta}–π^*_{HL})L_{tta}MCT
	H − 2 (A) → LUMO (A) (40%),	0.314	3.70	335	IL(π_{tta}–π^*_{tta})LLCT(π_{tta}–π^*_{HL})L_{tta}MCT
	H − 1 (A) → L + 1 (A) (33%)				
	H − 1 (A) → L + 2 (A) (23%)	0.215	3.80	326	IL(π_{tta}–π^*_{tta})LLCT(π_{tta}–π^*_{HL})L_{tta}MCT
complex 5	H − 1 (A) → LUMO (A) (42%)	0.132	3.51	354	IL(π_{tta}–π^*_{tta})LLCT($\pi_{\text{hydrazide group}}$–$\pi^*_{tta}$) L_{tta}MCT
	H − 1 (A) → L + 1 (A) (27%)	0.366	3.57	347	IL(π_{tta}–π^*_{tta})LLCT($\pi_{\text{hydrazide group}}$–$\pi^*_{tta}$)
	H − 3 (A) → LUMO (A) (15%),	0.792	3.59	345	IL(π_{tta}–π^*_{tta})LLCT(π_{HL}–π^*_{tta})L_{tta}MCT
	HOMO (A) → L + 2 (A) (26%)				IL(π_{HL}–π^*_{HL})
	H − 2 (A) → LUMO (A) (24%)	0.106	3.60	344	IL(π_{tta}–π^*_{tta})LLCT(π_{HL}–π^*_{tta})L_{tta}MCT
	H − 2 (A) → LUMO (A) (29%)	0.158	3.61	343	IL(π_{tta}–π^*_{tta})LLCT(π_{HL}–π^*_{tta})L_{tta}MCT
	H − 4 (A) → L + 1 (A) (25%)	0.208	3.80	326	IL(π_{tta}–π^*_{tta})LLCT($\pi_{\text{hydrazide group}}$–$\pi^*_{tta}$) LMCT
	H − 3 (A) → L + 1 (A) (15%)	0.362	3.85	322	IL(π_{tta}–π^*_{tta})LLCT($\pi_{\text{hydrazide group}}$–$\pi^*_{tta}$) LMCT
	H − 4 (A) → L − + − 1 (A) (20%)	0.193	3.89	319	IL(π_{tta}–π^*_{tta})LLCT($\pi_{\text{hydrazide group}}$–$\pi^*_{tta}$) LMCT

complex,[35] in which photoisomerization of the stilbene group was suppressed owing to the presence of LLCT $\pi_{HL} \rightarrow \pi^*_{tfd}$ and the absence of backward LLCT $\pi_{tfd} \rightarrow \pi^*_{HL}$. This resulted in complex [Eu(tfd)$_2$(HL) (CF$_3$COO)] having a higher sensitization efficiency of 97.9% in the acetonitrile solution and 96.7% in the solid state, making the isomerization reaction difficult to observe and the quantum yield too low to be detected. This study shows that complex 3 has good dual photoisomerization and photoluminescence functions owing to its lower sensitization efficiency.

Complex 4 showed the largest contribution from the LLCT (tta to HL) transition, which favored the energy transfer from tta to HL and promoted photoisomerization. Furthermore, energy transfer from the ligands to the gadolinium ion was

inhibited, resulting in complex 4 showing the largest photoisomerization quantum yield. The transition characteristic of complex 5 was slightly different from those of complexes 1−4 but similar to that of the tfd-coordinated complex [Yb(tfd)$_2$(HL)]. The LLCT transition between ligands mainly originated from the hydrazide group in HL to the tta ligand, while the LLCT from tta to HL ($\pi_{tta} \rightarrow \pi^*_{HL}$) was absent. The LMCT transition mainly originated from the tta ligand to the central Yb^{3+} ion. Therefore, the luminescence and trans-to-cis photoisomerization properties of complex 5 were similar to those of complex [Yb(tfd)$_2$(HL)].

CONCLUSIONS

Five new di-β-diketonate lanthanide complexes co-coordinated with a stilbene derivative were synthesized and characterized. The crystals of the five complexes belonged to the monoclinic $P2_1/c$ space group. For complexes **1−4**, the central lanthanide ion was nine-coordinate with a monocapped twisted square antiprism polyhedron geometry. The central Yb(III) ion of complex **5** was eight-coordinate with a distorted double-capped triangular prism polyhedron geometry. The photo-induced trans-to-cis isomerization properties of the five complexes in acetonitrile solutions showed that their photo-isomerization rate constants (k_{iso}) and quantum yields (Φ_{t-c}) and those of the free ligand HL were in the order of **4 > 3 > 5 > 2 > 1 >** HL. Complex **4** showed the best photoisomerization properties accompanied by magnetic properties. Complex **3** showed reversible luminescence change upon the trans-to-cis photoisomerization process. Such complexes are promising substitutes for pure ligands in molecular switch applications. The magnitude of the trans-to-cis isomerization yield and rate constant of these complexes and the sensitization efficiency of ligand energy transfer to the lanthanide ion were attributed to the extent of the ligand-to-ligand charge-transfer transition from HL to tta ($\pi_{HL} \rightarrow \pi^*_{tta}$) and ligand-to-metal energy transfer.

EXPERIMENTAL SECTION

Materials and Methods. $LnCl_3 \cdot 6H_2O$ (Ln = La, Nd, Eu, Gd, and Yb) was purchased from Beijing Huawei Ruike Co. Htta and 2-(chloromethyl)pyridine hydrochloride were obtained from Alfa Aesar, and all other chemicals were purchased from Sinopharm Chemicals Group Co. The melting point was determined using an X-4 micromelting point apparatus (Shanghai Precision Scientific Instrument Co. Ltd.) without correction. Electrospray ionization (ESI)−mass spectrometry (MS) was performed using a Bruker ESQUIRE-3000 Plus liquid chromatography−MS/MS spectrometer. Elemental analysis was performed using a Vario EL III elemental analyzer. TGA was conducted using an SDT Q600 thermogravimetric analyzer under a nitrogen atmosphere with a heating rate of 10 °C/min. Solution ^{1}H-NMR spectra were acquired using a Bruker ADVANCE 400 spectrometer at 400 MHz and 25 °C with tetramethylsilane as the internal reference. IR spectra (KBr pellets) were obtained using a Nicolet AVATAR FT-IR 330 spectrometer. Absorption spectra were recorded using a Shimadzu UV224012PC absorption spectrometer. Luminescence spectra were obtained using a Hitachi F7000 fluorescence spectrophotometer at room temperature with excitation and emission slits set at 2.5 and 5.0 nm, respectively. The overall quantum yields of the compounds were determined in the organic solvent at room temperature using the emission quantum yield (Φ = 0.028) of $Ru(bpy)_2Cl_2$ using an air-saturated aqueous solution as the standard.[70] Solid sample luminescence quantum yields and lifetimes were determined using an Edinburgh instruments FLS980 fluorescence spectrometer equipped with a Hamamatsu R5509 NIR photomultiplier tube, and excitation and emission slits were set to 2.0 and 5.0 nm, respectively. Magnetic measurements were conducted at a sweep rate of 1.5 K min^{-1} on a Quantum Design SQUID XL7 magnetometer over a temperature range of 2−300 K. When measuring photoisomerization quantum yields, UV light (254 and 312 nm) was acquired from a Shanghai Yihui ZF-2 UV analyzer.

This type of analyzer can emit radiation at wavelengths of 254, 312, and 365 nm. The light intensity was measured using a UV-A radiation meter (Optical Electrical Apparatus Factory, Beijing Normal University). Photoirradiation experiments were performed in acetonitrile solutions using a UV analyzer. A quartz cell with a light path length of 10 mm was used for photoisomerization measurements. The concentration of all complexes was 2.0×10^{-5} mol L^{-1}. The photoisomerization quantum yield (φ_{iso}) and trans-to-cis first-order kinetics isomerization rate constant (k_{iso}) were calculated using previously reported methods.[34] The quantum yields and rate constants were averages of three measurements and data errors were within 10%.

Syntheses of the Co-Coordinated Stilbene Ligand (HL) and Lanthanide(III) Complexes 1−5 (Scheme 1). HL was prepared in exactly the same way as the previous synthesized method.[35] The lanthanide complexes were synthesized as follows: 0.42 g of ligand HL (1.0 mmol) and 0.30 g of Htta (2.5 mmol) were mixed and dissolved in 20 mL of tetrahydrofuran. After the mixed compounds were completely dissolved, 1 M sodium hydroxide solution was added dropwise slowly to the solution to adjust the pH to about 7. It should be pointed out that some of the Htta ligand is hydrolyzed to produce the CF_3COO^- anion in the system. After that, the solution was heated to 65 °C, and 1.0 mmol $LnCl_3 \cdot 6H_2O$ in 5 mL of methanol solution was added and allowed to stand for refluxing for 10 h. Then, the solution was filtered while hot, and the resulting solution was rotated to obtain the solids. The solid powder was washed and dried to obtain pure lanthanide complexes. The pure solid powder was dissolved in methanol and then filtered, and the solution was allowed to stand in the dark to volatilize. Crystals were obtained after 1 week.

[La(tta)$_2$(HL) (CF$_3$COO)] (1). Light yellow crystal, yield: 70% (0.76 g); ESI(+)-MS: m/z (CH$_3$OH) = 1001.0 [M$^+$]; ^{1}H NMR (400 MHz, DMSO-d_6): δ (ppm) 9.68 (s, 1 H), 8.49 (s, 2 H), 7.84 (dd, J = 7.4, 8 H), 7.62 (m, 5H), 7.38−7.16 (m, 10 H), 6.28 (s, 2 H), 4.30 (s, 4 H); FT-IR (cm^{-1}): 3214, 3062 (C=C−H, m), 1680 (C=O, s), 1610 (C=C, s), 1538 (N−H, m), 1344, 1285(C−N, s), 1178, 1127 (C−F, s), 943 (C−S−C, s) 783, 711, 641 (Ph−H, w); elemental analysis calculated for LaC$_{45}$H$_{32}$F$_9$N$_4$O$_7$S$_2$ (%): N, 5.03; C, 48.48; H, 2.89; S, 5.75; found (%): N, 5.01; C, 48.39; H, 3.06; S, 5.70.

[Nd(tta)$_2$(HL) (CF$_3$COO)] (2). Light lavender crystal, yield:72% (0.80 g); ESI(+)-MS: m/z (CH$_3$OH) = 1006.0 [M$^+$]; FT-IR (cm^{-1}): 3209 (C=C−H, m), 1680 (C=O, s), 1614 (C=C, s), 1539 (N−H, m), 1414, 1311 (C−N, s), 1178, 1135 (C−F, s), 933 (C−S−C, s), 757, 683, 641 (Ph−H, w): elemental analysis calculated for NdC$_{45}$H$_{32}$F$_9$N$_4$O$_7$S$_2$ (%): N, 5.01; C, 48.25; H, 2.88; S, 5.73; found (%): N, 5.07; C, 47.52; H, 2.93; S, 5.72.

[Eu(tta)$_2$(HL) (CF$_3$COO)] (3). Yellow crystal, yield: 65% (0.78 g); ESI(+)-MS: m/z (CH$_3$OH) = 1015.0 [M$^+$]; ^{1}HNMR (400 MHz, DMSO-d_6): δ (ppm) 9.66 (s, 1 H), 8.47 (s, 2 H), 7.75−7.62 (m, 9H), 7.37−7.25 (m, 7H), 6.47−6.37 (s, 4H), 4.52−4.29 (m, 6 H); FT-IR(cm^{-1}): 3177 (C=C−H, m), 1689 (C=O, s), 1621 (C=C, s), 1538 (N−H, m), 1412, 1303 (C−N, s), 1185, 1137 (C−F, s), 933 (C−S−C), 785, 706, 641 (Ph−H, w); elemental analysis calculated for EuC$_{45}$H$_{32}$F$_9$N$_4$O$_7$S$_2$ (%): N, 4.97; C, 47.92; H, 2.86; S, 5.69; found (%): N, 4.95; C, 47.33; H, 2.77; S, 5.63.

[Gd(tta)$_2$(HL) (CF$_3$COO)] (4). Transparent crystal, yield: 75% (0.83 g); ESI(+)-MS: m/z (CH$_3$OH) = 1020.0 [M$^+$]; FT-

IR (cm^{-1}): 3208, 3025 (C≡C−H, m), 1688(C=O, s), 1613 (C=C, s), 1538(N−H, m), 1412, 1297 (C−N, s), 1178, 1138 (C−F, s), 934(C−S−C, s) 783, 711, 641 (Ph−H, w); elemental analysis calculated for GdC$_{45}$H$_{32}$F$_9$N$_4$O$_7$S$_2$ (%): N, 4.94; C, 47.70; H, 2.85; S, 5.66; found (%): N, 4.95; C, 47.50; H, 2.62; S, 5.58.

[Yb(tta)$_2$(L)] (5). Transparent crystal, yield: 55% (0.56 g); ESI(+)-MS: m/z (CH$_3$OH) = 1036.0 [M$^+$]; FT-IR (cm^{-1}): 3032, 2915 (C≡C−H, m), 1686 (C=O, s), 1631 (C=C, s), 1545 (N−H, m), 1412, 1304 (C−N, S), 1187, 1143 (C−F, s), 933(C−S−C, s), 766, 700, 643 (Ph−H, w); elemental analysis calculated for YbC$_{43}$H$_{31}$F$_6$N$_4$O$_5$S$_2$ (%): N, 5.41; C, 49.90; H, 3.02; S, 6.20; found (%): N, 5.42; C, 49.37; H, 2.93; S, 6.26.

Structural Determination of Complexes 1−5 by X-ray Diffraction. Structural determination of complexes 1−5 was performed using X-ray diffraction. Single-crystal X-ray diffraction data of the five complexes were collected using a Rigaku Oxford Diffraction XtaLAB Synergy diffractometer with micro-focus sealed X-ray Cu Kα radiation (λ = 1.54184 Å) at 100 K. Crystallography data reduction and absorption correction were performed using CrysAlisPro 171.41_64.110a software (Rigaku Oxford Diffraction, 2015). The structures were solved by intrinsic phasing (SHEXT) and refined by full-matrix least-squares calculations based on F^2 using the SHELXTL-2014 software package.[71,72] All non-hydrogen atoms were refined anisotropically. The disordered solvent in the structures was removed using the PLATON SQUEEZE program.[73] Crystallographic details for complexes 1−5 are summarized in Table 1.

Theoretical calculations. Ground-state structures of the five complexes were optimized in the acetonitrile solvent using DFT. The solvent was simulated using the PCM. In our previous report on HL-related lanthanide complexes, the Cam-B3lYP functional combined with default MWD28 specified for the SDD [Stuttgart Dresden triple zeta ECPs] basis set was found to correlate well with the experimental absorption spectra.[35] In the present study, the SDD basis set was again selected, and both the B3lYP and CAM-B3LYP functionals were used to model the electronic structures of complexes. However, the B3LYP functional was found to yield results more consistent with the observed properties of the complexes. Therefore, the B3LYP functional was used, the 6−31(g) basis set was selected for elements C, H, O, N, S, and F, and relativistic ECP and segmented basis sets were used for lanthanide ions. Optimized structures were verified by frequency calculations to check that the energy minimum was reached. The optimized ground-state structure was then used to calculate the singlet and triplet excitation energies of the five complexes, and their electronic spectra were calculated using TD−DFT. The G16 package was used for all calculations. A free GaussSum program was selected to analyze the molecular orbitals.[74]

ASSOCIATED CONTENT

SI Supporting Information

The Supporting Information is available free of charge at https://pubs.acs.org/doi/10.1021/acsomega.1c05557.

> Selected bond lengths and angles for complexes 1−5; selected bond lengths and angles for complexes 1−5 optimized by DFT method; crystal structure and coordination polyhedron geometry of complexes 1, 2, and 3; experimental and simulated X-ray powder

diffraction patterns of complexes 1−5; TGA curves of complexes 1−5; UV-Vis spectral changes of complexes 1, 2, 4, and 5 in acetonitrile solutions upon irradiation and recoverable irradiation as a function of time; CIE color coordinates of complex 3; luminescence decay curves of complex 3 in an acetonitrile solution and in the solid state; cycle number of the maximum luminescence intensity of complex 3 modulated by irradiation of UV light; phosphorescence spectra of Htfd, Htta, and their Gd complexes in acetonitrile solutions; ESI mass spectra of complexes 1−5 in methanol solution; ^{1}H NMR spectra of complexes 1 and 2 in DMSO-d_6; and IR spectra of complexes 1−5 and HL in KBr pellets (PDF)

CCDC 2111389−2111393 contain the supplementary crystallographic data for this paper. These data can be obtained free of charge via www.ccdc.cam.ac.uk/data_-request/cif, or by emailing data_request@ccdc.cam.a-c.uk Crystallographic data for La-1-2111389 (CIF) Crystallographic data for Eu-3-2111391 (CIF) Crystallographic data for Nd-2-2111390 (CIF) Crystallographic data for Yb-5-2111393 (CIF) Crystallographic data for Gd-4-2111392 (CIF)

AUTHOR INFORMATION

Corresponding Author

Li-Rong Lin − *Department of Chemistry, College of Chemistry and Chemical Engineering, Xiamen University, Xiamen 361005, P. R. China;* ⓘ orcid.org/0000-0002-2521-3809; Email: linlr@xmu.edu.cn

Authors

Han Xu − *Department of Chemistry, College of Chemistry and Chemical Engineering, Xiamen University, Xiamen 361005, P. R. China*

Yu Tan − *Department of Chemistry, College of Chemistry and Chemical Engineering, Xiamen University, Xiamen 361005, P. R. China*

Ziting Hou − *Department of Chemistry, College of Chemistry and Chemical Engineering, Xiamen University, Xiamen 361005, P. R. China*

Caiye Fu − *Department of Chemistry, College of Chemistry and Chemical Engineering, Xiamen University, Xiamen 361005, P. R. China*

Complete contact information is available at:
https://pubs.acs.org/10.1021/acsomega.1c05557

Author Contributions

[†]H.X. and Y.T. contributed equally to this work.

Notes

The authors declare no competing financial interest.

REFERENCES

(1) Dattler, D.; Fuks, G.; Heiser, J.; Moulin, E.; Perrot, A.; Yao, X.; Giuseppone, N. Design of Collective Motions from Synthetic Molecular Switches, Rotors, and Motors. *Chem. Rev.* 2020, 120, 310−433.

(2) Li, J.; Bisoyi, H. K.; Lin, S.; Guo, J.; Li, Q. 1,2-Dithienyldicyanoethene-Based, Visible-Light-Driven, Chiral Fluorescent Molecular Switch: Rewritable Multimodal Photonic Devices. *Angew. Chem., Int. Ed.* **2019**, *58*, 16052−16056.

(3) Martynov, A. G.; Safonova, E. A.; Tsivadze, A. Y.; Gorbunova, Y. G. Functional Molecular Switches Involving Tetrapyrrolic Macrocycles. *Coord. Chem. Rev.* **2019**, *387*, 325−347.

(4) Suda, M.; Thathong, Y.; Promarak, V.; Kojima, H.; Nakamura, M.; Shiraogawa, T.; Ehara, M.; Yamamoto, H. M. Light-driven molecular switch for reconfigurable spin filters. *Nat. Commun.* **2019**, *10*, 245−251.

(5) Wang, H.; Bisoyi, H. K.; Urbas, A. M.; Bunning, T. J.; Li, Q. Reversible Circularly Polarized Reflection in a Self-Organized Helical Superstructure Enabled by a Visible-Light-Driven Axially Chiral Molecular Switch. *J. Am. Chem. Soc.* **2019**, *141*, 8078−8082.

(6) Zhang, Y.; Zhou, Y.; Gao, T.; Yan, P.; Li, H. Metal-directed synthesis of quadruple-stranded helical Eu(iii) molecular switch: a significant improvement in photocyclization quantum yield. *Chem. Commun.* **2020**, *56*, 13213−13216.

(7) Devi, R.; Rajendran, M.; Singh, K.; Pal, R.; Vaidyanathan, S. Smart Luminescent Molecular Europium Complexes and Their Versatile Applications. *J. Mater. Chem. C* **2021**, *9*, 6618−6633.

(8) Boddula, R.; Tagare, J.; Singh, K.; Vaidyanathan, S. White Light-Emissive Europium Complexes and Their Versatile Applications. *Mater. Chem. Front.* **2021**, *5*, 3159−3175.

(9) Devi, R.; Vaidyanathan, S. Narrow Band Red Emitting Europium Complexes and Their Application in Smart White Leds and Vapoluminescent Sensors. *Dalton Trans.* **2020**, *49*, 6205−6219.

(10) Ma, L.; Li, C.; Yan, Q.; Wang, S.; Miao, W.; Cao, D. Unsymmetrical photochromic bithienylethene-bridge tetraphenylethene molecular switches: Synthesis, aggregation-induced emission and information storage. *Chin. Chem. Lett.* **2020**, *31*, 361−364.

(11) Areephong, J.; Browne, W. R.; Katsonis, N.; Feringa, B. L. Photo- and electro-chromism of diarylethene modified ITO electrodes - towards molecular based read-write-erase information storage. *Chem. Commun.* **2006**, 3930−3932.

(12) Gao, Z.; Han, Y.; Wang, F. Cooperative supramolecular polymers with anthracene. endoperoxide photo-switching for fluorescent anti-counterfeiting. *Nat. Commun.* **2018**, *9*, 3977−3985.

(13) Zhang, Z.; Ma, N.; Yao, S.; Han, W.; Li, X.; Chang, H.; Wang, Y.-Y. Transparent and Hazy EuxTb1-x-Nanopaper with Color-Tuning, Photo-Switching, and White Light-Emitting Properties for Anti-counterfeiting and Light-Softened WLEDs. *ACS Sustain. Chem. Eng.* **2021**, *9*, 5827−5837.

(14) Yan, D.; Wang, Z.; Cheng, P.; Chen, Y.; Zhang, Z. Rational Fabrication of Crystalline Smart Materials for Rapid Detection and Efficient Removal of Ozone. *Angew. Chem., Int. Ed.* **2021**, *60*, 6055−6060.

(15) García-Calvo, J.; Vallejos, S.; García, F. C.; Rojo, J.; García, J. M.; Torroba, T. A smart material for the in situ detection of mercury in fish. *Chem. Commun.* **2016**, *52*, 11915−11918.

(16) Alam, R.; Lightcap, I. V.; Karwacki, C. J.; Kamat, P. V. Sense and Shoot: Simultaneous Detection and Degradation of Low-Level Contaminants Using Graphene-Based Smart Material Assembly. *ACS Nano* **2014**, *8*, 7272−7278.

(17) Zhang, H.; Fan, T.; Chen, W.; Li, Y.; Wang, B. Recent advances of two-dimensional materials in smart drug delivery nano-systems. *Bioact. Mater.* **2020**, *5*, 1071−1086.

(18) Wang, X.; Cheng, R.; Cheng, L.; Zhong, Z. Lipoyl Ester Terminated Star PLGA as a Simple and Smart Material for Controlled Drug Delivery Application. *Biomacromolecules* **2018**, *19*, 1368−1373.

(19) Das Mahapatra, S.; Mohapatra, P. C.; Aria, A. I.; Christie, G.; Mishra, Y. K.; Hofmann, S.; Thakur, V. K. Piezoelectric Materials for Energy Harvesting and Sensing Applications: Roadmap for Future Smart Materials. *Adv. Sci.* **2021**, *7*, 25−44.

(20) Kampes, R.; Zechel, S.; Hager, M. D.; Schubert, U. S. Halogen bonding in polymer science: towards new smart materials. *Chem. Sci.* **2021**, *12*, 9275−9286.

(21) Shen, S.; Wu, T.; Xue, J. J.; Li, H. X.; Chen, Q. S.; Cheng, H. Y.; Wu, L.; Qian, J. A smart material built upon the photothermochromic effect and its use for managing indoor temperature. *Chem. Commun.* **2021**, *57*, 8628−8631.

(22) Wei, H.; Gu, J. X.; Ren, F. F.; Zhang, L. P.; Xu, G. P.; Wang, B.; Song, S. S.; Zhao, J. P.; Dou, S. L.; Li, Y. Smart Materials for Dynamic Thermal Radiation Regulation. *Small* **2021**, *17*, 3410−3422.

(23) Wieszczycka, K.; Staszak, K.; Woźniak-Budych, M. J.; Litowczenko, J.; Maciejewska, B. M.; Jurga, S. Surface functionalization - The way for advanced applications of smart materials. *Coord. Chem. Rev.* **2021**, *436*, 213846−213867.

(24) Yang, M.; Wang, S.-Q.; Liu, Z.; Chen, Y.; Zaworotko, M. J.; Cheng, P.; Ma, J.-G.; Zhang, Z. Fabrication of Moisture-Responsive Crystalline Smart Materials for Water Harvesting and Electricity Transduction. *J. Am. Chem. Soc.* **2021**, *143*, 7732−7739.

(25) Andréasson, J.; Pischel, U. Smart molecules at work-mimicking advanced logic operations. *Chem. Soc. Rev.* **2010**, *39*, 174−188.

(26) Yang, P.; Zhu, F.; Zhang, Z.; Cheng, Y.; Wang, Z.; Li, Y. Stimuli-responsive polydopamine-based smart materials. *Chem. Soc. Rev.* **2021**, *50*, 8319−8343.

(27) Bandara, H. M. D.; Burdette, S. C. Photoisomerization in different classes of azobenzene. *Chem. Soc. Rev.* **2012**, *41*, 1809−1825.

(28) Yan, Y.; Wang, X.; Chen, J. I. L.; Ginger, D. S. Photoisomerization Quantum Yield of Azobenzene-Modified DNA Depends on Local Sequence. *J. Am. Chem. Soc.* **2013**, *135*, 8382−8387.

(29) Bronner, C.; Priewisch, B.; Rück-Braun, K.; Tegeder, P. Photoisomerization of an Azobenzene on the Bi(111) Surface. *J. Phys. Chem. C* **2013**, *117*, 27031−27038.

(30) Fu, C.-Y.; Chen, L.; Wang, X.; Lin, L.-R. Synthesis of Bis-beta-Diketonate Lanthanide Complexes with an Azobenzene Bridge and Studies of Their Reversible Photo/Thermal Isomerization Properties. *ACS Omega* **2019**, *4*, 15530−15538.

(31) Fujiwara, M.; Imura, T. Photo Induced Membrane Separation for Water Purification and Desalination Using Azobenzene Modified Anodized Alumina Membranes. *ACS Nano* **2015**, *9*, 5705−5712.

(32) Singleton, T. A.; Ramsay, K. S.; Barsan, M. M.; Butler, I. S.; Barrett, C. J. Azobenzene Photoisomerization under High External Pressures: Testing the Strength of a Light-Activated Molecular Muscle. *J. Phy. Chem. B* **2012**, *116*, 9860−9865.

(33) Wang, C.; Hashimoto, K.; Tamate, R.; Kokubo, H.; Morishima, K.; Li, X.; Shibayama, M.; Lu, F.; Nakanishi, T.; Watanabe, M. Viscoelastic change of block copolymer ion gels in a photo-switchable azobenzene ionic liquid triggered by light. *Chem. Commun.* **2019**, *55*, 1710−1713.

(34) Lin, L.-R.; Tang, H.-H.; Wang, Y.-G.; Wang, X.; Fang, X.-M.; Ma, L.-H. Functionalized Lanthanide(III) Complexes Constructed from Azobenzene Derivative and beta-Diketone Ligands: Luminescent, Magnetic, and Reversible Trans-to-Cis Photoisomerization Properties. *Inorg. Chem.* **2017**, *56*, 3889−3900.

(35) Chen, L.; Tan, Y.; Xu, H.; Wang, K.; Chen, Z.-H.; Zheng, N.; Li, Y.-Q.; Lin, L.-R. Enhanced E/Z-photoisomerizationr and luminescence of stilbene derivative co-coordinated in di-beta-diketonate lanthanide complexes. *Dalton Trans.* **2020**, *49*, 16745−16761.

(36) Ge, Y.; Ando, N.; Liu, L.; Wang, X.; Sauriol, F.; Yamaguchi, S.; Wu, G.; Wang, S. Multistep Photoisomerization of Dimesitylboron-Functionalized Stilbene Analogues. *Org. Lett.* **2020**, *22*, 3258−3262.

(37) van den Berg, J. L.; Neumann, K. I.; Harrison, J. A.; Weir, H.; Hohenstein, E. G.; Martinez, T. J.; Zare, R. N. Strong, Nonresonant Radiation Enhances Cis-Trans Photoisomerization of Stilbene in Solution. *J. Phys. Chem. A* **2020**, *124*, 5999−6008.

(38) Amaral, R. C.; Iha, N. Y. M. Molecular engineered rhenium(i) carbonyl complexes to promote photoisomerization of coordinated stilbene-like ligands in the visible region. *Dalton Trans.* **2018**, *47*, 13081−13087.

(39) Feofanov, M.; Uka, A.; Akhmetov, V.; Amsharov, K. Photocyclization of diarylethenes with a boronate moiety: a useful

synthetic tool to soluble PAH building blocks. *Photochem. Photobiol. Sci.* **2020**, *19*, 722−725.

(40) Cao, J.; Wang, G.; Gao, L.; Cheng, X.; Li, S. Organocatalytic reductive coupling of aldehydes with 1,1-diarylethylenes using an in situ generated pyridine-boryl radical. *Chem. Sci.* **2018**, *9*, 3664−3671.

(41) Irie, M.; Fukaminato, T.; Matsuda, K.; Kobatake, S. Photochromism of Diarylethene Molecules and Crystals: Memories, Switches, and Actuators. *Chem. Rev.* **2014**, *114*, 12174−12277.

(42) Su, Y. L.; Dong, K.; Zheng, H.; Doyle, M. P. Generation of Diazomethyl Radicals by Hydrogen Atom Abstraction and Their Cycloaddition with Alkenes. *Angew. Chem., Int. Ed.* **2021**, *60*, 18484−18488.

(43) Ma, J.; Chen, S.; Bellotti, P.; Guo, R.; Schäfer, F.; Heusler, A.; Zhang, X.; Daniliuc, C.; Brown, M. K.; Houk, K. N.; Glorius, F. Photochemical intermolecular dearomative cycloaddition of bicyclic azaarenes with alkenes. *Science* **2021**, *371*, 1338−1345.

(44) Joannou, M. V.; Hoyt, J. M.; Chirik, P. J. Investigations into the Mechanism of Inter- and Intramolecular Iron-Catalyzed [2+2] Cycloaddition of Alkenes. *J. Am. Chem. Soc.* **2020**, *142*, 5314−5330.

(45) Taura, D.; Urushima, A.; Sugioka, Y.; Ousaka, N.; Yashima, E. Remote-controlled regio- and diastereodifferentiating photodimerization of a dynamic helical peptide-bound 2-substituted anthracene. *Chem. Commun.* **2020**, *56*, 13433−13436.

(46) Tanabe, J.; Taura, D.; Ousaka, N.; Yashima, E. Chiral Template-Directed Regio-, Diastereo-, and Enantioselective Photodimerization of an Anthracene Derivative Assisted by Complementary Amidinium-Carboxylate Salt Bridge Formation. *J. Am. Chem. Soc.* **2017**, *139*, 7388−7398.

(47) Maturi, M. M.; Fukuhara, G.; Tanaka, K.; Kawanami, Y.; Mori, T.; Inoue, Y.; Bach, T. Enantioselective [4+4] photodimerization of anthracene-2,6-dicarboxylic acid mediated by a C-2-symmetric chiral template. *Chem. Commun.* **2016**, *52*, 1032−1035.

(48) Manchester, J.; Bassani, D. M.; Duprey, J.-L. H. A.; Giordano, L.; Vyle, J. S.; Zhao, Z.-y.; Tucker, J. H. R. Photocontrolled Binding and Binding-Controlled Photochromism within Anthracene-Modified DNA. *J. Am. Chem. Soc.* **2012**, *134*, 10791−10794.

(49) Irie, M. Photochromism: Memories and switches - Introduction. *Chem. Rev.* **2000**, *100*, 1683.

(50) Donthamsetti, P. C.; Broichhagen, J.; Vyklicky, V.; Stanley, C.; Fu, Z.; Visel, M.; Levitz, J. L.; Javitch, J. A.; Trauner, D.; Isacoff, E. Y. Genetically Targeted Optical Control of an Endogenous G Protein-Coupled Receptor. *J. Am. Chem. Soc.* **2019**, *141*, 11522−11530.

(51) Gascón-Moya, M.; Pejoan, A.; Izquierdo-Serra, M.; Pittolo, S.; Cabré, G.; Hernando, J.; Alibés, R.; Gorostiza, P.; Busqué, F. An Optimized Glutamate Receptor Photoswitch with Sensitized Azobenzene Isomerization. *J. Org. Chem.* **2015**, *80*, 9915−9925.

(52) Goudet, C.; Rovira, X.; Llebaria, A. Shedding light on metabotropic glutamate receptors using optogenetics and photopharmacology. *Curr. Opin. Pharmacol.* **2018**, *38*, 8−15.

(53) Herrera-Arozamena, C.; Estrada-Valencia, M.; Martí-Marí, O.; Pérez, C.; de la Fuente Revenga, M.; Villalba-Galea, C. A.; Rodríguez-Franco, M. I. Optical control of muscular nicotinic channels with azocuroniums, photoswitchable azobenzenes bearing two N-methyl-N-carbocyclic quaternary ammonium groups. *Eur. J. Med. Chem.* **2020**, *200*, 112403.

(54) Hüll, K.; Morstein, J.; Trauner, D. In Vivo Photopharmacology. *Chem. Rev.* **2018**, *118*, 10710−10747.

(55) Yamauchi, M.; Yamamoto, S.; Masuo, S. A Highly Ordered Quantum Dot Supramolecular Assembly Exhibiting Photoinduced Emission Enhancement. *Angew. Chem., Int. Ed.* **2021**, *60*, 6473−6479.

(56) Zhang, M.; Yan, X.; Huang, F.; Niu, Z.; Gibson, H. W. Stimuli-Responsive Host-Guest Systems Based on the Recognition of Cryptands by Organic Guests. *Accounts Chem. Res.* **2014**, *47*, 1995−2005.

(57) Lin, L.-R.; Wang, X.; Wei, G.-N.; Tang, H.-H.; Zhang, H.; Ma, L.-H. Azobenzene-derived tris-beta-diketonate lanthanide complexes: reversible trans-to-cis photoisomerization in solution and solid state. *Dalton Trans.* **2016**, *4S*, 14954−14964.

(58) Wang, Y.-G.; Li, Y.-Q.; Tang, H.-H.; Lin, L.-R.; Ma, L.-H. Near-Infrared Photoluminescence and Reversible Trans-to-Cis Photoisomerization of Mononuclear and Binuclear Ytterbium(III) Complexes Functionalized by Azobenzene Groups. *ACS Omega* **2018**, *3*, 5480−5490.

(59) Singh, K.; Boddula, R.; Vaidyanathan, S. Versatile Luminescent Europium(III)-beta-Diketonate-imidazo-bipyridyl Complexes Intended for White LEDs: A Detailed Photophysical and Theoretical Study. *Inorg. Chem.* **2017**, *56*, 9376−9390.

(60) Eliseeva, S. V.; Bünzli, J.-C. G. Lanthanide luminescence for functional materials and bio-sciences. *Chem. Soc. Rev.* **2010**, *39*, 189−227.

(61) Zhang, H.; Li, N.; Tian, C.; Liu, T.; Du, F.; Lin, P.; Li, Z.; Du, S. Unusual High Thermal Stability within a Series of Novel Lanthanide Tatb Frameworks: Synthesis, Structure, and Properties (Tatb=4,4 ',4 "-S-Triazine-2,4,6-Triyl-Tribenzoate). *Cryst. Growth Des.* **2012**, *12*, 670−678.

(62) Akhtar, M. N.; Chen, Y.-C.; AlDamen, M. A.; Tong, M.-L. 3d Oxalato-Bridged Lanthanide(Iii) Mofs with Magnetocaloric, Magnetic and Photoluminescence Properties. *Dalton Trans.* **2017**, *46*, 116−124.

(63) Zanoni, K. P. S.; Murakami Iha, N. Y. Reversible Trans Reversible Arrow Cis Photoisomerizations of [Re(Co)₃(Ph)₂(Phen)-(Stpycn)](+) Towards Molecular Machines. *Dalton Trans.* **2017**, *46*, 9951−9958.

(64) Amaral, R. C.; Matos, L. S.; Zanoni, K. P. S.; Iha, N. Y. M. Photoreversible Molecular Motion of Stpycn Coordinated to Fac-[Re(Co)(3)(Nn)](+) Complexes. *J. Phys. Chem. A* **2018**, *122*, 6071−6080.

(65) Werts, M. H. V.; Jukes, R. T. F.; Verhoeven, J. W. The Emission Spectrum and the Radiative Lifetime of Eu3+ in Luminescent Lanthanide Complexes. *Phys. Chem. Chem. Phys.* **2002**, *4*, 1542−1548.

(66) He, H.; Zhu, X.; Hou, A.; Guo, J.; Wong, W.-K.; Wong, W.-Y.; Li, K.-F.; Cheah, K.-W. Reactivity of Aqua Coordinated Monoporphyrinate Lanthanide Complexes: Synthetic, Structural and Photoluminescent Studies of Lanthanide Porphyrinate Dimers. *Dalton Trans.* **2004**, *23*, 4064−4073.

(67) Klink, S. I.; Hebbink, G. A.; Grave, L.; Van Veggel, F. C. J. M.; Reinhoudt, D. N.; Slooff, L. H.; Polman, A.; Hofstraat, J. W. Sensitized near-Infrared Luminescence from Polydentate Triphenylene-Functionalized Nd³⁺,Yb³⁺, and Er³⁺ Complexes. *J. Appl. Phys.* **1999**, *86*, 1181−1185.

(68) Khan, L. U.; Brito, H. F.; Hölsä, J.; Pirota, K. R.; Muraca, D.; Felinto, M. C. F. C.; Teotonio, E. E. S.; Malta, O. L. Red-Green Emitting and Superparamagnetic Nanomarkers Containing Fe3o4 Functionalized with Calixarene and Rare Earth Complexes. *Inorg. Chem.* **2014**, *53*, 12902−12910.

(69) Gavriluta, A.; Fix, T.; Nonat, A.; Slaoui, A.; Guillemoles, J.-F.; Charbonnière, L. J. Tuning the Chemical Properties of Europium Complexes as Downshifting Agents for Copper Indium Gallium Selenide Solar Cells. *J. Mat. Chem. A* **2017**, *5*, 14031−14040.

(70) Brouwer, A. M. Standards for Photoluminescence Quantum Yield Measurements in Solution (Iupac Technical Report). *Pure Appl. Chem.* **2011**, *83*, 2213−2228.

(71) Sheldrick, G. M. Shelxt - Integrated Space-Group and Crystal-Structure Determination. *Acta Crystallogr., Sect. A: Found. Adv.* **2015**, *71*, 3−8.

(72) Sheldrick, G. M. Crystal Structure Refinement with Shelxl. *Acta Crystallogr., Sect. C: Struct. Chem.* **2015**, *71*, 3−8.

(73) Spek, A. L. Platon Squeeze: A Tool for the Calculation of the Disordered Solvent Contribution to the Calculated Structure Factors. *Acta Crystallogr., Sect. C: Struct. Chem.* **2015**, *71*, 9−18.

(74) O'boyle, N. M.; Tenderholt, A. L.; Langner, K. M. cclib: A library for package-independent computational chemistry algorithms. *J. Comput. Chem.* **2008**, *29*, 839−845.